Simulation of Motor-Driven Cochlear Outer Hair Cell Electromotility

Alexander A. Spector, Mohammed Ameen, and Aleksander S. Popel

Department of Biomedical Engineering, Center for Computational Medicine and Biology and Center for Hearing Sciences, Johns Hopkins University, Baltimore, Maryland 21205 USA

ABSTRACT   We propose a three-dimensional (3D) model to simulate outer hair cell electromotility. In our model, the major components of the composite cell wall are explicitly represented. We simulate the activity of the particles/motor complexes in the plasma membrane by generating active strains inside them and compute the overall response of the cell. We also consider the constrained wall and compute the generated active force. We estimate the parameters of our model by matching the predicted longitudinal and circumferential electromotile strains with those observed in the microchamber experiment. In addition, we match the earlier estimated values of the active force and cell wall stiffness. The computed electromotile strains in the plasma membrane and other components of the wall are in agreement with experimental observations in trypsinized cells and in nonmotile cells transfected with Prestin. We discover several features of the 3D mechanism of outer hair cell electromotilty. Because of the constraints under which the motors operate, the motor-related strains have to be 2–3 times larger than the observable strains. The motor density has a strong effect on the electromotile strain. Such effect on the active force is significantly lower because of the interplay between the active and passive properties of the cell wall.

INTRODUCTION

Outer hair cells are receptor/effector cells located in the mammalian cochleae. These cells are critically important for the active processes in the cochlea that result in the active amplification and sharp frequency selectivity of the ear. Outer hair cells also contribute to the cochlear nonlinearities that are subject to clinical tests for normal or pathological conditions of the inner ear. Elongated cylindrical outer hair cells have a unique form of motility, changing their length and radius in response to changes of the cell membrane electric potential. Such dimensional changes of the cell do not require ATP or Ca^{2+}, common factors in cell motility of a biochemical origin. As a reciprocal phenomenon to the electromotile dimensional changes, constrained outer hair cells generate active forces up to frequencies of tens of thousands of Hertz when subjected to electrical excitation (Frank et al., 1999). Electromotility was first observed in isolated cells (Brownell et al., 1985). As was shown later, mechanical (Evans and Dallos, 1993) or electrical (Mammano and Ashmore, 1993; Xue et al., 1993) stimulation of outer hair cells in the intact cochlea that causes the cell's electromotile response can drive vibration of the basilar membrane. It was also shown in living cochleae that the application of drugs known to diminish outer hair cell electromotility cause loss of amplification, sharpness of the frequency selectivity, and cochlear nonlinearities (Ruggero and Rich, 1991).

The molecular basis and the site of the motors driving outer hair cell electromotility have been a subject of intensive studies. The outer hair cell has a liquid core bounded by a composite wall. The cell wall is a trilaminar structure with the innermost component, called subsurface cisternae, the outermost plasma membrane, and the cytoskeleton sandwiched between the two (Brownell et al., 2001). Treatment of the cell wall with trypsin digesting the cytoskeleton does not eliminate cell electromotility (Kalinec et al., 1992). Also, electrical patch clamping of the plasma membrane in both cell-attached and detached modes showed electromotile responses within the patches (Kalinec et al., 1992; Gale and Ashmore, 1997). This led to a hypothesis that the plasma membrane is the site of the motors responsible for outer hair cell motility (Kalinec et al., 1992; Iwasa, 1994; Holley, 1996). The plasma membrane includes an array of particles identified by freeze fracture electron microscopy and embedded in the plasma membrane with a density unusually high for intramembranous proteins. The electromotile response of the outer hair cell is associated with an electric charge transferred across the cell wall (Santos-Sacchi and Digler, 1988; Ashmore, 1990). The transferred charge and the cell length changes as functions of the cell membrane potential are qualitatively similar. The distribution of the particles along the plasma membrane is nonuniform, with lower densities in the areas adjacent to the cell ends (Forge, 1991). Experiments show (Gale and Ashmore, 1997) that the transferred charge in those areas is also small. Estimates of the density of the hypothetical motors (Ashmore, 1990; Iwasa, 1994) associated with the transferred charge are reasonably close to that for the particles in the plasma membrane, although this correspondence has recently been challenged for shorter cells (Santos-Sacchi et al., 1998).

Geleoc et al. (1999) have proposed a sugar transporter as a candidate for the molecular motor, a view challenged by developmental experimental measurements (Belyanseva et al., 2000). Zheng et al. (2000) have identified the outer hair

cell molecular motor with a newly discovered protein called Prestin. When Prestin is expressed in human kidney cells, they exhibit electromotile response and nonlinear capacitance, features typical for the active outer hair cell. In addition, it has been shown that the electromotile response of kidney cell with Prestin can be reduced by salicylate, an agent inhibiting outer hair cell electromotility. Belyanseva et al. (2000) have confirmed that, during cell development, Prestin appears at the same time as cell electromotlity. Ludwig et al. (2001) have recently shown that originally nonmotile cells transfected with Prestin have other features of outer hair cell electromotility, including the active force production in the acoustic range of frequencies and a tension-dependent shift of nonlinear capacitance. A number of observations, such as the densities of the particles, transferred charge, and Prestin molecules close to each other, show that the molecular motors driving outer hair cell electromotility are associated with the particles in the plasma membrane. However, the actual arrangement of the particles/motor complexes, including the number of Prestin units, their relative motion during conformational changes, and conversion of the transmembrane displacement of the electric charge into in-plane dimensional changes of the motor complex, have yet to be understood.

Dallos et al. (1993) have proposed a theoretical model to relate the activity of hypothetical molecular motors to the overall electromotile response of the outer hair cell. They represented the cell wall as a network of identical elastic springs connected to two-dimensional (2D) two-state electrically activated motors. Dallos et al. (1993) and Hallworth et al. (1993) fit the length and radius changes observed in the microchamber experiment by choosing the parameters of the motor conformational changes and the stiffness of the passive springs. Iwasa (1994, 1996) has effectively represented the cell wall as a passive continuum matrix with two- or three-state motors whose area changes have been related to the overall electromotile response of the cell. In that model, the motors could be activated both electrically and mechanically.

Proposing an alternative flexoelectric-type mechanism of electromotility, Raphael et al. (2000) have developed a model where outer hair cell motility is driven by plasma membrane curvature changes in response to electrically-evoked reorientation of hypothetical dipoles in the plasma membrane. Jen and Steele (1987) have proposed a model of an electrokinetic mechanism of electromotility when the cell is driven by longitudinal forces developed as a result of the application of the electric field to charges distributed within cell wall.

Spector et al. (1998a) have proposed a continuum model of the passive properties of the outer hair cell wall with an explicit representation of the major components of the composite wall. The plasma membrane and the subsurface cisterna were modeled by isotropic shells. The cytoskeleton and the radial pillars were modeled by an orthotropic shell and by a set of elastic springs, respectively. Later, Spector (2001) developed a continuum model of the composite outer hair cell wall where the electrically active plasma membrane was connected to the passive elastic layer that included the cytoskeleton and the subsurface cisterna.

In the present paper, we use the available information on the cell's wall nanostructure and simulate the three-dimensional (3D) motor-related mechanism of cell motility. We take into account the major components of the cell wall and computationally simulate the process of the electrical excitation of the particles/motor complexes accompanied by the active strain and force transmission throughout the wall. Some of the parameters of the model, such as the stiffness of the cytoskeleton, are taken from the available experimental data or previous theoretical estimates. Other parameters are determined as a result of matching the experimental values of the elecromotile strains and active forces produced by the whole cell. In our modeling of the electromotile strains, we assume that no external mechanical forces are applied to the cell wall. Because of this, we compare our results with measurements from the microchamber experiment where the effect of the mechanical resultants is minimal. On the basis of our modeling of the 3D composite wall structure, we estimate the longitudinal and circumferential components of the active strains electrically generated in particles/motors as 11% and −4%, respectively, resulting in a motor area change of 7%. The motor-related strains are redistributed within the wall by the passive component of the particles, lipid bilayer surrounding the particles, and (to a smaller extent) by the passive cytoskeleton and subsurface cisternae connected to the plasma membrane. As a result of such redistribution, the limiting values of the longitudinal and circumferential components of the overall electromotile strain in the wall reduce, respectively, to 5% and −2%, the values observed in the microchamber experiment. We show that the electromotile response of the composite cell wall (and the whole cell) is primarily determined by that of the plasma membrane. This is in agreement with observations in trypsinized cells, cells with altered connections between the plasma membrane and the cytoskeleton, and originally nonmotile (kidney) cells transfected with Prestin. We investigate the effect of the particle/motor complex density on the active properties of the cell. We show that the density effect on the electromotile strain is strong. Such effect on the active force production is much weaker because of the interplay between the active and passive properties of the cell wall.

MATHEMATICAL MODEL OF THE COMPOSITE OUTER HAIR CELL WALL

We start with the major components of the composite outer hair cell wall and present the constitutive relations describing the behavior of each of these components. Then we

define the overall strains, stiffness, and active force that characterize the effective passive and active properties of the whole wall. The effective characteristics of the wall are obtained as a result of a two-step analysis. First, the limiting values that correspond to fully excited array of particles/motor complexes are determined. Then, we find the active and passive characteristics at arbitrary electric potential when only a fraction of the motor complexes is excited.

The outer hair cell wall consists of three major layer-type components: the plasma membrane, cytoskeleton, and subsurface cisternae. There is a space between the cytoskeleton and the plasma membrane (extracisternal space) penetrated by radial pillars connecting these two components of the wall. In the present paper, we develop a quasistatic analysis of the cell wall where the effect of the fluid in the extracisternal space reduces to a hydrostatic pressure; because the extracisternal space and the cell core are connected (Brownell and Popel, 1998) the extracisternal pressure is equal to that inside the cell core. In the dynamic (high frequency) analysis, the motion and interaction with the wall components of the fluids inside and outside the cell have a significant effect on the cell mechanics and electromotility (Tolomeo and Steele, 1998, Ratnanather et al., 1997). A dynamic version of the current model is a subject of future research.

The cytoskeleton and the subsurface cisterna appear to be closely associated, and, because of this, perfect bonding of these two components is assumed in the model given below. If later experimental data show significant slip or relative displacement of the cytoskeleton and the subsurface cisterna, then the model can be easily modified by the introduction of a layer connecting the two components of the composite wall. The subsurface cisternae is a stack of lipid bilayers, and its arrangement does not appear to favor any direction that would result in anisotropy of mechanical properties. The cytoskeleton is composed of actin filaments connected by shorter and thinner spectrin crosslinks. The cytoskeleton is arranged as a composition of microdomains of different size and orientation (Holley et al., 1992). Such a nanostructure makes the cytoskeleton effectively stiffer in the circumferential direction. Tolomeo et al. (1996) measured the longitudinal and circumferential stiffness of an isolated cytoskeleton. Spector et al. (2000) analyzed the relation between the effective stiffness of the cytoskeleton and its nanostructure. They estimated the components of the full matrix of anisotropy for the cytoskeleton and matched the longitudinal and circumferential stiffness of Tolomeo et al. (1996). The plasma membrane is composed of a lipid bilayer and an array of densely packed solid particles. Qualitative observations of a domain-type arrangement of the plasma membrane have been reported (Kalinec and Kachar, 1995); however, these observations do not yet provide quantitative geometric data that can be used in simulation of electromotility. For this reason, we make an assumption of a uniform distribution of the particles along the plasma membrane. The main components of the composite outer hair cell wall entering our model are shown in Fig. 1.

We represent the subsurface cisternae, cytoskeleton, and plasma membrane by linear elastic shells and represent the radial pillars by linear elastic springs. The springs have the stiffness in the longitudinal and circumferential directions, and they cause forces acting on the plasma membrane and the cytoskeleton. These forces are proportional to the relative displacements of the plasma membrane and the cytoskeleton in the circumferential and longitudinal directions.

FIGURE 1   General view of the outer hair cell and an element of the composite wall of the cell. The main components of the cell wall are: the innermost subsurface cisterna (1), the outermost plasma membrane (3) with embedded particles (4), and the cytoskeleton sandwiched between them (2). The plasma membrane is connected to the cytoskeleton by a system of radial pillars (5).
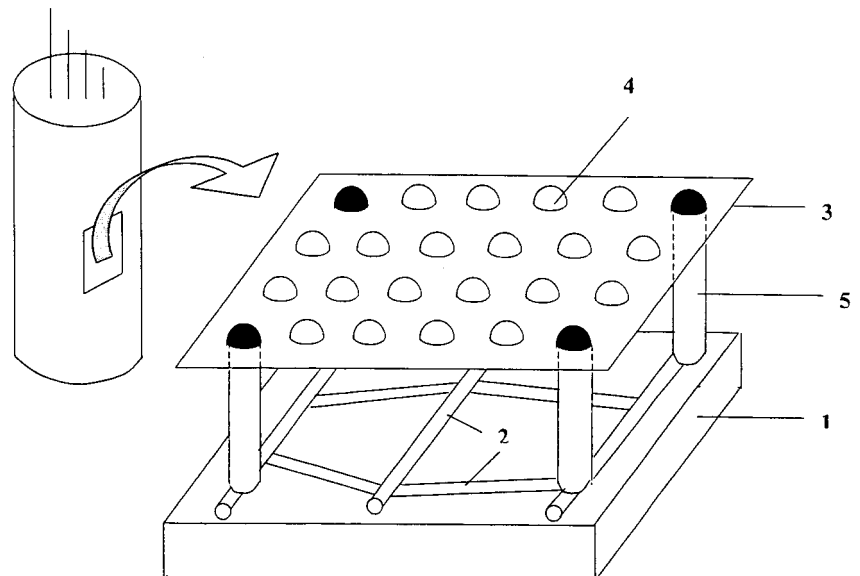
The resultant forces and strains in the subsurface cisternae and the cytoskeleton are given by the equations of 2D linear elasticity (e.g., Love, 1952)

$$N_x^1 = \frac{E^1 h^1}{1 - (v^1)^2} \varepsilon_x^1 + \frac{v^1 E^1 h^1}{1 - (v^1)^2} \varepsilon_\theta^1, \tag{1}$$

$$N_\theta^1 = \frac{v^1 E^1 h^1}{1 - (v^1)^2} \varepsilon_x^1 + \frac{E^1 h^1}{1 - (v^1)^2} \varepsilon_\theta^1, \tag{2}$$

$$N_x^2 = C_{11}^2 \varepsilon_x^1 + C_{12}^2 \varepsilon_\theta^1, \tag{3}$$

$$N_\theta^2 = C_{12}^2 \varepsilon_x^1 + C_{22}^2 \varepsilon_\theta^1. \tag{4}$$

Here, superscripts 1 and 2 correspond, respectively, to the subsurface cisternae and cytoskeleton; N_x and N_θ are, respectively, components of the resultant forces; ε_x and ε_θ are, respectively, longitudinal and circumferential components of the in-plane strain; E^1, v^1, and h^1 are, respectively, in-plane Young's modulus, Poisson's ratio, and the thickness of the subsurface cisternae; and C_{11}^2, C_{12}^2, and C_{22}^2 are the coefficients of the in-plane stiffness of the cytoskeleton. Eqs. 1–4 reflect isotropy of the subsurface cisternae and anisotropy of the cytoskeleton as well as perfect bonding ($\varepsilon_x^1 = \varepsilon_x^2$ and $\varepsilon_\theta^1 = \varepsilon_\theta^2$) of these two components of the composite wall.

Constitutive relations for the material between particles in the plasma membrane (lipid bilayer populated by other proteins) take the form

$$N_x^3 = \frac{E^3 h^3}{1 - (v^3)^2} \varepsilon_x^3 + \frac{v^3 E^3 h^3}{1 - (v^3)^2} \varepsilon_\theta^3, \tag{5}$$

$$N_\theta^3 = \frac{v^3 E^3 h^3}{1 - (v^3)^2} \varepsilon_x^3 + \frac{E^3 h^3}{1 - (v^3)^2} \varepsilon_\theta^3. \tag{6}$$

Here, superscript 3 corresponds to the plasma membrane; E^3 and v^3 are, respectively, Young's modulus and Poisson's ratio of the lipid bilayer, and h^3 is the thickness of the plasma membrane. For the lipid bilayer in the plasma membrane, we use the model of an isotropic slightly compressible (in terms of the surface area) elastic material. The small compressibility of the lipid bilayer in the plasma membrane is represented by the relationships

$$K^3/\mu^3 \gg 1 \quad \text{or} \quad v^3 \to 1, \tag{7}$$

where

$$K^3 = \frac{E^3}{2(1 - v^3)} \quad \text{and} \quad \mu^3 = \frac{E^3}{2(1 + v^3)} \tag{8}$$

are, respectively, area expansion modulus and shear modulus.

We assume that each particle is made of a 2D elastic isotropic material. We simulate the conformational change of the motor complex associated with the particle by generating 2D uniform initial strain. This strain plays the role of active strain produced by an individual motor complex in response to the cell membrane potential change. The total strains within the particles are the sum of the elastic passive strains and the active strains occurring in response to the application of the electric field. The introduction of motor-related active strain is convenient in terms of the description of the motor activity. Such strain can be associated with the motor complex area change and the relative motion of the protein domains that accompanies the conformational changes. For the material within the particles, the constitutive relations between the membrane forces and strains are chosen in the form similar to the piezoelectric-type relationships (e.g., Spector et al., 1999)

$$N_x^p = \frac{E^p h^3}{1 - (v^p)^2} (\varepsilon_x^p - \varepsilon_x^0) + \frac{v^p E^p h^3}{1 - (v^p)^2} (\varepsilon_\theta^p - \varepsilon_\theta^0), \tag{9}$$

$$N_\theta^p = \frac{v^p E^p h^3}{1 - (v^p)^2} (\varepsilon_x^p - \varepsilon_x^0) + \frac{E^p h^3}{1 - (v^p)^2} (\varepsilon_\theta^p - \varepsilon_\theta^0). \tag{10}$$

Here, E^p and v^p are, respectively, Young's modulus and Poisson's ratio of the material of the particles, and ε_x^0 and ε_θ^0 are, respectively, the longitudinal and circumferential components of the active strain generated within the particles.

We assume a periodic arrangement of the cell wall in both longitudinal and circumferential directions. Under this assumption, pillars are separated by distance d_x in the x direction and d_θ in the θ direction. Thus, the wall surface can be represented as a composition of identical units with two pillars and a number of particles/motor complexes shown in Fig. 2 A. In our simulation of the electromotile strains, we consider the case where no external forces are applied to the cell wall, and the whole electromotile response of the cell wall is determined by the strains generated within the particles. For all units composing the wall, the strain components as well as the circumferential and normal components of the displacement are the same. The longitudinal component of the displacement is accumulated along the cell and is proportional to the number of units included into consideration in the x direction.

Because of the symmetry of the original unit (Fig. 2 A), our consideration reduces to the analysis of a half of the unit as shown in Fig. 2 B. The final unit includes one pillar ending at the middle particle in the front row. On the basis of the symmetry of the original unit, double periodicity of the strains in the wall, and zero-mechanical forces applied to the cell wall, we use the following set of boundary conditions

$$u_x = 0, \quad N_{x\theta} = 0 \quad \text{along side1} \tag{11}$$

$$N_{x\theta} = 0, \quad u_x = \text{const} \quad \text{along side2} \tag{12}$$

$$u_\theta = 0, \quad N_{x\theta} = 0 \quad \text{along side3} \tag{13}$$

$$N_{x\theta} = 0, \quad u_\theta = \text{const} \quad \text{along side4} \tag{14}$$
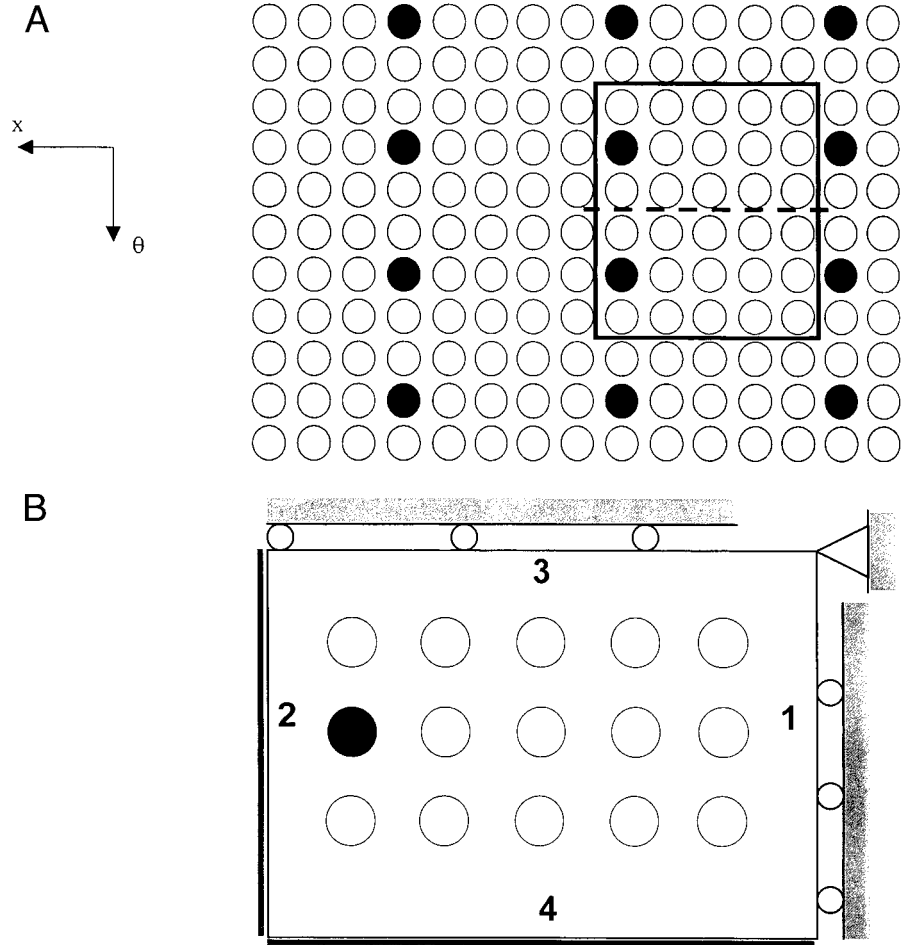
A

x

θ

FIGURE 2   (*A*) *X*- and *θ*-periodic structure representing the outer hair cell wall. Circles represent particles/motor complexes in the plasma membrane. Closed circles correspond to the projections of the radial pillars. (*B*) Basic unit of the mathematical model and computational procedure. Circles represent particles in the plasma membrane. Closed circle corresponds to the projection of a single radial pillar of the unit. The rollers along sides 1 and 3 of the unit illustrate the zero-tangential-resultant boundary conditions. The bars along sides 2 and 4 illustrate the constant-displacement boundary conditions.

B

Here, u_x and u_θ are, respectively, the longitudinal and circumferential components of the in-plane displacement, and $N_{x\theta}$ is the shear component of the resultant. In addition to these conditions, the periodicity in the x direction results in the constraint

$$u_\theta(\theta, \text{side1}) = u_\theta(\theta, \text{side2}), \qquad (15)$$

and the periodicity in the θ direction results in the constraint

$$u_x(x, \text{side3}) = u_x(x, \text{side4}). \qquad (16)$$

The boundary conditions are schematically illustrated in Fig. 2 *B*. The conditions $u_x = \text{const}$ along side 2 and $u_\theta = \text{const}$ along side 4 are illustrated in Fig. 2 *B* by imaginary rigid bars acting on sides 2 and 4 of the unit. These constant displacement conditions result in some N_x and N_θ forces along sides 2 and 4, respectively. However, the overall forces applied to any side of the unit are equal to zero. After the determination of the displacement components, we calculate the overall electromotile strains as

$$\varepsilon_x = \frac{u_x}{d_x}, \quad \varepsilon_\theta = \frac{u_\theta}{d_\theta}. \qquad (17)$$

We also introduce the active force produced by the cell wall under isometric conditions. Such active force is defined as the resultant corresponding to zero electromotile strains. To find the isometric active force on the basis of our model, we impose $u_x = 0$ and $u_\theta = 0$ conditions along sides 2 and 4, respectively. After that, the longitudinal f_x^* and circumferential f_θ^* components of the active force are, respectively, equal to such resultants N_x (side 2) and N_θ (side 4) that provide the above conditions for the displacements u_x and u_θ.

In addition to the active force and active strain, we consider the overall passive stiffness of the wall. The passive stiffness of the wall is determined under the conditions when there is no active strain generated in the particles ($\varepsilon_x^0 = \varepsilon_\theta^0 = 0$). Because of orthotropy of the cytoskeleton, the whole wall exhibits orthotropic properties characterized by moduli C_{11}, C_{12}, and C_{22}. To determine moduli C_{11} and C_{12}, we apply resultants N_x along side 2 and N_θ along side 4. These resultants are chosen to provide zero displacement u_θ along side 4. The ratios of N_x and N_θ to the corresponding strain ε_x give, respectively, moduli C_{11} and C_{12}. To determine modulus C_{22}, we apply such resultants N_x and N_θ that

provide zero displacement u_x along side 2. The ratio of the resultant N_θ to the corresponding strain ε_θ gives modulus C_{22}.

We assume that each motor complex can be in one of two states: activated ($\varepsilon_x^0 \neq 0$, $\varepsilon_\theta^0 \neq 0$) and inactivated ($\varepsilon_x^0 = 0$, $\varepsilon_\theta^0 = 0$) with the probabilities $p(\Delta\Psi)$ and $1 - p(\Delta\Psi)$, respectively, determined by the membrane potential $\Delta\Psi$. The overall strain of the unit and the whole wall is determined by accumulation of the strains caused by the excitation of the particles/motor complexes. If we have the limiting values of the strains corresponding to the fully excited array of the particles, then the strains for a partially excited array should be proportional to the fraction of the excited particles. Taking into account the properties of binomial distribution that the fraction of the excited particles obeys, the strains for a partially excited array can be represented by the equations

$$\varepsilon_x(\Delta\Psi) = \varepsilon_x^* M(\Delta\Psi) = \varepsilon_x^* p(\Delta\Psi), \quad (18)$$

$$\varepsilon_\theta(\Delta\Psi) = \varepsilon_\theta^* M(\Delta\Psi) = \varepsilon_\theta^* p(\Delta\Psi), \quad (19)$$

where the coefficients ε_x^* and ε_θ^* correspond to the limiting conditions when all particles are excited, and $M(\Delta\Psi)$ is the mean value of the fraction of excited particles for the given potential. Thus, as follows from Eqs. 18–19, simulation of the active strain reduces to computation of the limiting values corresponding to the fully excited array of particles. The active strain at arbitrary electric potential is simply obtained by multiplication of the limiting values by $p(\Delta\Psi)$, prescribed function of the potential. The active force is determined as a result of a similar procedure.

The proposed model is valid for any function $p(\Delta\Psi)$ describing the probability of the motor complex being in the activated state, the model can be generalized to cases of more than two states of the motor complex. In our simulation, following Dallos et al. (1993) and Iwasa (1994 and 1996), we use the Boltzmann distribution given by the expression

$$p(\Delta\Psi) = \frac{\exp[(\Delta\Psi - \Delta\Psi^0)/b]}{1 + \exp[(\Delta\Psi - \Delta\Psi^0)/b]}. \quad (20)$$

COMPUTATIONAL PROCEDURE

The finite element method is used for analyzing the basic unit of the outer hair cell wall. Nine-node isoparametric quadrilateral plane stress elements are used to model the subsurface cisterna, the cytoskeleton, and the plasma membrane. The pillars are modeled by means of a pair of spring elements. The stiffness of these springs represent the stiffness of the pillar considered as a beam with fixed ends.

Because the computer memory and time requirements needed to discretize the plasma membrane unit is found to be large, we make use of the concept of substructuring (Cook et al., 1989). Each particle along with the surrounding material is discretized as shown in Fig. 3 A to form a super element. The degrees of freedom corresponding to all the internal nodes, except the nodes along the periphery of the circle forming the particle, are removed by static condensation (Fig. 3 B). These super-elements are then assembled as if they are ordinary finite elements. The internal degrees of freedom, which are condensed out initially, are recovered later to calculate the stresses and strains in the particle and the surrounding material.

The special boundary conditions (as explained earlier) are incorporated by assigning the same node numbers to those nodes that should have the same magnitude of displacement. However, care needs to be given to use the actual nodal coordinates in the formulation of the element matrices. The subsurface cisternae, cytoskeleton, and plasma membrane are discretized by using 15 super elements. The fine mesh for the plasma membrane includes 136 elements for each super element. The total number of equations is about 2500. The system is solved by the Gaussian elimination method taking into account its bandedness and symmetry.

Before developing the analysis of the whole composite computational unit, we check our finite element approach (and the corresponding code) against several test problems. First, we consider a square element that represents an isolated particle with a piece of the surrounding lipid bilayer. We generate an active strain in the particle and analyze the
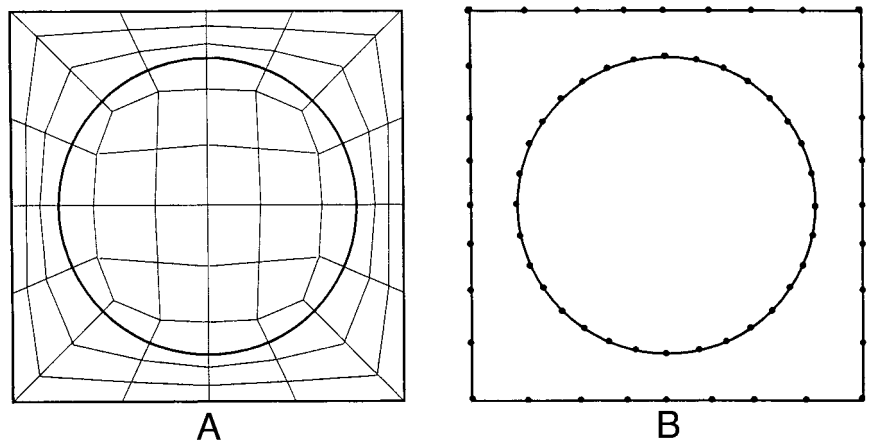

FIGURE 3 Finite element analysis. (A) Detailed discretization of a typical super element in the plasma membrane by using 9-node quadrilateral finite elements. (B) Nodes at which the degrees of freedom are retained on the super element.

A

B

resulting node displacements in the surrounding material. We repeat this analysis by using different meshes and show the convergence of the results. We do similar analysis for the part of the unit that belongs to the plasma membrane. We also check our results against those obtained by using the finite element package ABAQUS (Hibbitt, Karlsson & Sorensen, Inc, Pawtucket, RI).

Figure 4 shows the computational unit before and after excitation of the particles/motor complexes. The boundaries of the unit and of the particles corresponding to the inactivated (undeformed) state are given by dotted lines. The boundaries of the unit and of the particles corresponding to fully excited particles are given by solid lines. Figure 4 also shows finite element mesh around one of the particles.

RESULTS

Major criteria for the model

We simulate the electromotile strain (active force) production and satisfy several criteria. The major criteria in our modeling are:

1. The electromotile strains in the cell wall should match the longitudinal and circumferential strains observed in the experiment with unconstrained motility (Dallos et al., 1993; Hallworth et al., 1993).
2. The isometric active force should match earlier estimates obtained on the basis of a continuum approach (Spector et al., 1999; Spector, 2001).
3. The stiffness of the composite wall should match our previous estimates obtained on the basis of a continuum approach (Spector et al., 1998b).
4. The stiffness of the cytoskeleton should correspond to its experimental measurements (Tolomeo et al., 1996).
5. The material surrounding the particles is slightly compressible (Poisson's ratio close to 1), and its stiffness (in terms of Young's modulus) is much smaller than that for the particles.

Parameters of the model

Some of the parameters of our model are unavailable from direct experiments or earlier theoretical estimates. These parameters are considered free parameters of the model and are chosen to match the criteria given above. The rest of the parameters are taken from available information on the cell wall nanostructure. The free parameters of the model are: the activation strains, ε_x^0 and ε_θ^0; the elastic moduli for the material surrounding the particles, E^3 and v^3; the passive elastic moduli for the material of the particles E^p and v^p; and the elastic moduli for the subsurface cisternae, E^1 and v^1. The geometric parameters used in our simulation are available from nanostructural measurements (Forge, 1991; Brownell and Popel, 1998, Brownell et al., 2001)

$$D_p = 10\text{nm}, \quad h_p = 25\text{nm}, \quad d = 12\text{nm},$$

$$l = 2\text{nm}, \quad h^1 = 50\text{nm}, \quad h^3 = 10\text{nm}, \quad (21)$$

where D_p and h_p are, respectively, the diameter and height of the pillar, and d and l are, respectively, the diameter of the particle and the edge-to-edge distance between neighboring particles. In addition to these basic values of d and l, we vary the parameters of the particle arrangement in the plasma membrane to investigate the effect of the motor complex density on electromotility. For the cell cytoskeleton, we use the results of direct measurements of its orthotropic moduli (Tolomeo et al., 1996)

$$C_{11}^2 = 4 \times 10^{-4} \text{ N/m},$$

$$C_{12}^2 = 2 \times 10^{-4} \text{ N/m},$$

$$C_{22}^2 = 2 \times 10^{-3} \text{ N/m} \quad (22)$$

The sensitivity analysis shows that Poisson's ratios, v^1 and v^p, are not significant parameters in terms of fitting

FIGURE 4 Deformation of the unit as a result of the excitation of the particles/motor complexes. Dotted lines correspond to the undeformed state. Solid lines correspond to the deformed state. Constant displacements along sides 2 and 4 determine the electroimotile response on the unit and whole cell. The area around one of the particles is discretized with the finite element mesh.
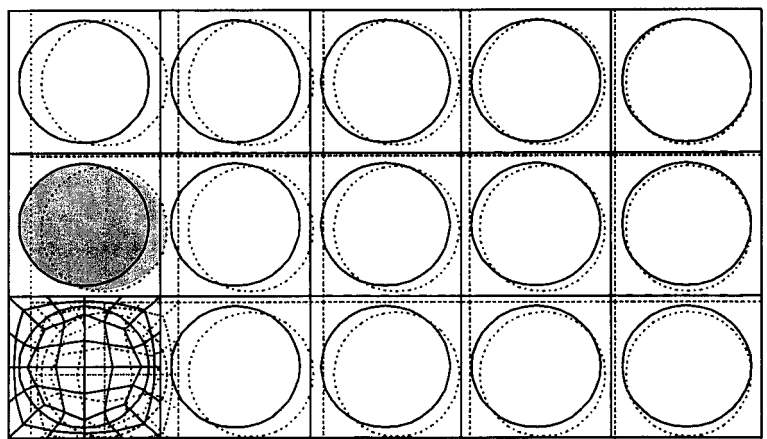
criteria 1–5, and they are chosen as

$$v^1 = 0.3, \quad v^p = 0.3. \quad (23)$$

Poisson's ratio v^3 determines the level of compressibility of the material around the particles. To characterize the small compressibility of the lipid bilayer, this modulus has to be close to 1, which is equivalent to the large ratio of the area modulus over the shear modulus (Eq. 7). Estimates of both area modulus and shear modulus for the lipid bilayer of the outer hair cell plasma membrane are unavailable. For this reason, we consider a range of values for v^3 close to unity. The sensitivity analysis shows that the values of the active strain and force change less than 20% when Poisson's ratio varies within the range

$$0.9 \leq v^3 \leq 0.999. \quad (24)$$

Further increase of the parameter v^3 causes computational instability with distortion of the finite element mesh. Thus, the largest value $v^3 = 0.999$ is chosen, which results in the ratio of two moduli for the lipid bilayer,

$$K^3/\mu^3 = 2 \times 10^3. \quad (25)$$

Results: Electromotile characteristics and elastic moduli of the wall components

After choosing the values of Poisson's ratios, the significant parameters reduce to two components of the activation strain and three Young's moduli for the subsurface cisternae, the particles, and the material around particles. These five parameters are determined as a result of the best fit of the limiting values of the circumferential and longitudinal electromotile strain, the longitudinal isometric active force, and the longitudinal stiffness of the cell wall. As a result of this fit, we obtain the following estimates of the longitudinal and circumferential component of the activation strain

$$\varepsilon_x^0 = 11\%, \quad \varepsilon_\theta^0 = -4\%. \quad (26)$$

The obtained membrane-type Young's moduli are given by the equations

$$E^1 h^1 = 3.5 \times 10^{-4} \text{ N/m},$$

$$E^p h^p = 70 \times 10^{-4} \text{ N/m},$$

$$E^3 h^3 = 3.5 \times 10^{-4} \text{ N/m}. \quad (27)$$

These values of the model parameters result in the following limiting values of the components of the active strain and the longitudinal active force:

$$\varepsilon_x^* = 4.8\%, \quad \varepsilon_\theta^* = -1.8\%, \quad (28)$$

and

$$f_x^* = 4.2 \times 10^{-3} \text{ N/m}. \quad (29)$$

We also compute the electromotile responses of the plasma membrane and cytoskeleton and find them close to each other. It indicates that the passive part of the cell wall is driven by the plasma membrane. We develop an additional computational experiment to investigate the role of the connections between the plasma membrane and the cytoskeleton. In this experiment, we compute the limiting electromotile response of the unit with a variable number of pillars that mimics electromotility of a cell with the altered density of the pillars. Figure 5 shows the patterns of the unit with the normal and greater numbers of pillars. The obtained longitudinal and circumferential components of the limiting electromotile strain are presented in Table 1.

We use the estimated limiting values of the electromotile strain and of the active force to obtain the potential dependence of the active characteristics of the wall. We present our results for different values of the parameter b of the Boltzmann function (Eq. 20). This parameter governs the rate of saturation of the active characteristics when they
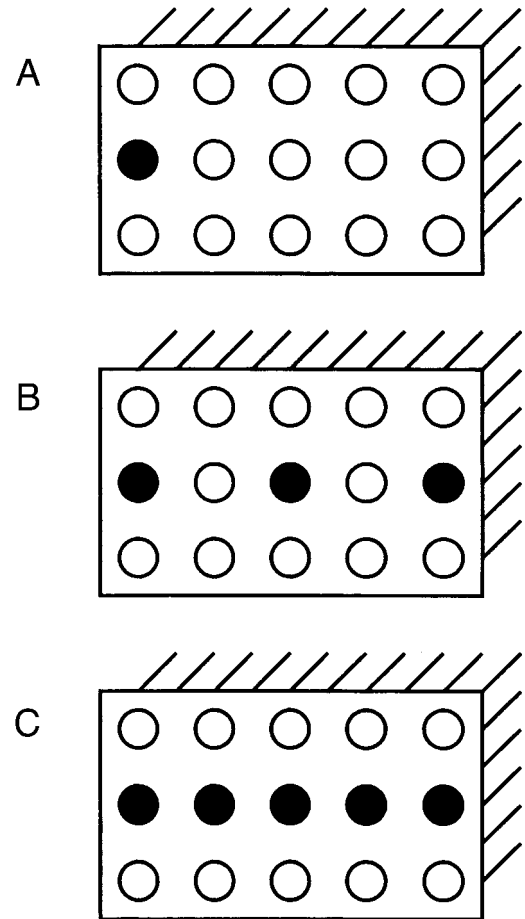

FIGURE 5   Analysis of the effect of the connections between the plasma membrane and cytoskeleton. Sketches show the computational units in the case (A) normal arrangement (one pillar per unit), (B) larger number of pillars (three pillars per unit) and (C) larger number of pillars (five pillars per unit).

approach their limiting values. We also analyze the effect of the particle/motor complex density in the plasma membrane. This density is varied by changing the distance between neighboring particles and keeping the diameter of the particle fixed. In Fig. 6 A, we present graphs for $b = 30$ mV for the longitudinal component of the electromotile strain against the cell membrane potential for three different values of the edge-to-edge distance between the particles. The curves 1, 2, and 3 correspond, respectively, to the edge-to-edge distances 2, 4, and 6 nm (densities of the particles are, respectively, 5100, 3900, and 3090 per μm^2). Figure 6, B and C, show similar sets of curves when the parameter b is equal to 50 and 65 mV, respectively. The curves in Fig. 7, A–C present the circumferential component of the electromotile strain for different values of the parameter b and the density of the particles. In similar fashion, Fig. 8, A–C present graphs for the longitudinal active force.

DISCUSSION

The graphs presented in Figs. 6, A–C and 7, A–C show the longitudinal and circumferential components of the electromotile strain in a broad range of the cell membrane potential around holding potential -70 mV. These results are obtained on the basis of simulation of unconstrained motility when no external mechanical forces are applied to the cell wall. We make comparison of our results with the data of microchamber experiment because this experiment allows measurements of two independent components of the electromotile strain under the condition of minimal perturbance of the resultants in the cell wall (Dallos et al., 1993).

The graphs in Figs. 6, A–C and 7, A–C capture the major features of the electromotile length and radius changes observed in the microchamber experiment (Dallos et al., 1993; Hallworth et al., 1993). These features include saturation of both strain components for extreme hyperpolarization or extreme depolarization and asymmetry with respect to the holding potential. The quantitative analysis of the available data on the cell length changes (Hallworth et al., 1993), represented in terms of the limiting values of the longitudinal strain results in the range

$$3.5\% \leq \varepsilon_x^* \leq 6\%. \tag{30}$$

This range reflects data from different cells and for different fractions of the cell included in the microchamber. Theoretical approximation of the experimental data proposed in Dallos et al. (1993) corresponds to the upper bound in Eq. 30. Our computational estimate (Eq. 28) falls within this range close to its middle point. Because there is a very limited pool of the direct experimental measurements of the electromotile radius change, we use theoretical fit of Dallos et al. (1993). The comparison shows that our estimate of the limiting value ε_θ^* (Eq. 28) is about 20–25% greater than that of Dallos et al. (1993). The predicted values used for these

TABLE 1 Electromotile responses of the plasma membrane for a variable number of pillars

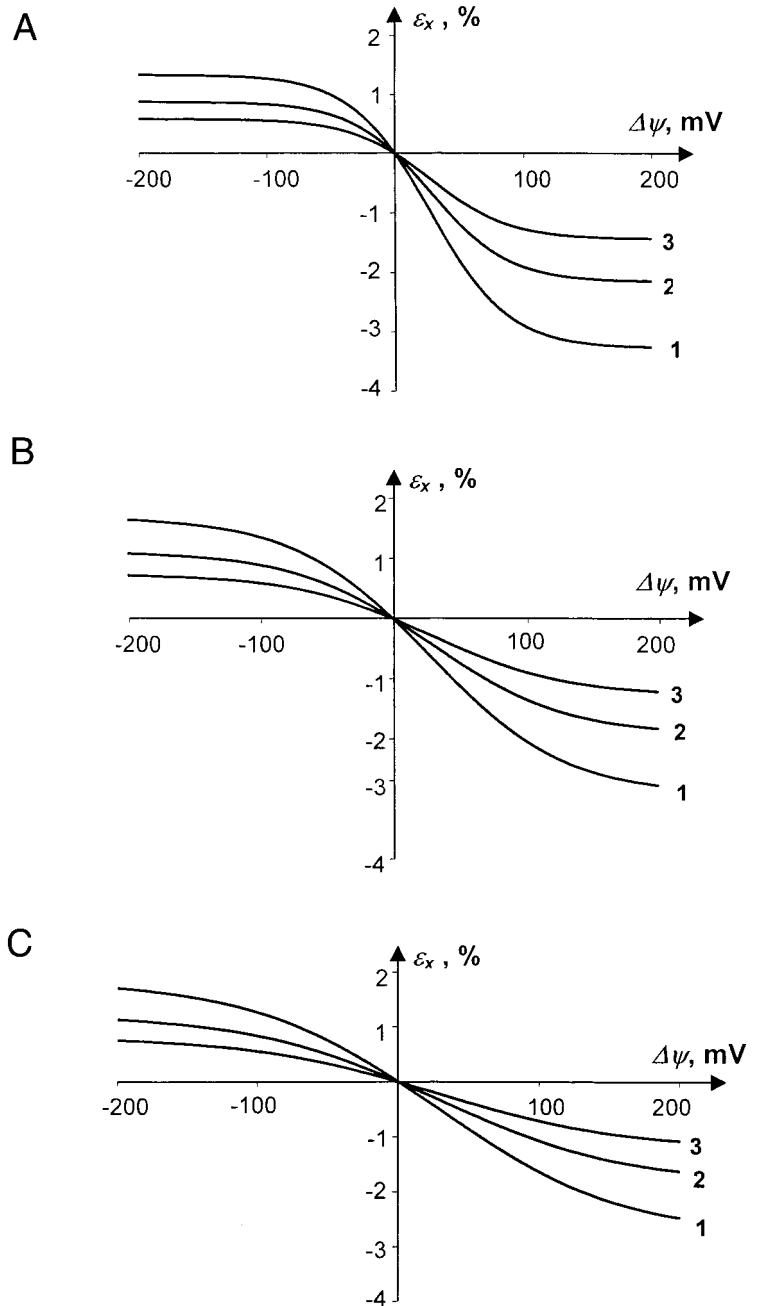| Number of Pillars	Longitudinal Component of the Electromotile Strain (%)	Circumferential Component of the Electromotile Strain (%)
1	4.8	−1.8
3	4.7	−1.79
5	4.6	−1.78

The effect of the connections between the plasma membrane and cytoskeleton is weak. This small effect consistently shows a slight increase in the absolute values of both the longitudinal and circumferential components of the electromotile strain.

comparisons correspond to the density of the motors given by $l = 2$ nm (5100 particles per μm^2).

The analysis of the computational unit (Figs. 4 and 5 and Table 1), both for the normal conditions and an altered number of pillars, shows that the electromotile response of the cell is primarily determined by the plasma membrane. The cytoskeleton has a weak effect on the response of the plasma membrane, which is in agreement with several experiments with trypsinized outer hair cells (Kalinec et al., 1992; Huang and Santos-Sacchi, 1994; Adachi and Iwasa, 1999), the original experiment with Prestin from gerbils (Zheng, 2000), and a new experiment with Prestin from rats (Ludwig et al., 2001). Moreover, our computations in the case of a variable number of pillars are in agreement with a specialized experiment where the cytoskeleton was treated in such a way that the connections between it and the plasma membrane were partially destroyed (F. Kalinec, personal communication). That treatment resulted in a slight increase in cell electromotility. Our data (Table 1) indicate a small but consistent increase in the absolute values of both the longitudinal and circumferential component of the electromotile strain. The cytoskeleton, however, is important to maintain the cylindrical shape of the cell and to provide turgor pressure inside the cell.

We estimate as 11% and −4% the motor-related strains that results in 7% area change of the motor switching to the activated state. There are transmembrane proteins whose conformational changes reach similar and even higher levels. Recently, Sukharev et al. (2001) studied the conformational changes of a 5×5 nm mechanosensitive multiple-state channel on the basis of measurements of conductance, data from the crystal structure, and molecular dynamics simulation. They found very significant area changes that are characterized by range 30–70% (see Fig. 2 in Sukharev et al., 2001), depending on which state, closed or closed/expanded, is compared with the open state. By using experimental data on the probability of the opening and closing of a stress-inactivated channel and a relation of their ratio to the channel's area change, Morris (1990) estimated area change greater than 5%. Morris also considered a stretch-activated channel and estimated its area change in the range 3–5%. The in-plane dimensions of those channels (9×9

A

B

FIGURE 6 The longitudinal component of the overall electromotile strain as a function of the cell wall potential for different values of the b parameter in the Boltzmann probability function of the motor being in the deformed state are considered. Also, the results for different motor densities, expressed in terms of the l edge-to-edge distance between particles, are shown. (A) $b = 30$ mV, $1 - l = 2$ nm, $2 - l = 4$ nm, and $3 - l = 6$ nm (corresponding densities of the particles are 5100, 3900, and 3090 particles per μm^2); (B) $b = 50$ mV, $1 - l = 2$ nm, $2 - l = 4$ nm, and $3 - l = 6$ nm; (c) $b = 65$ mV, $1 - l = 2$ nm, $2 - l = 4$ nm, and $3 - l = 6$ nm.

C

nm, Morris, 1990) were similar to the particle/motor complex in the outer hair cell wall. In their analysis of Prestin, Zheng et al. (2000) found its similarity to the family of transporters. The quantitative information on area changes in the transporters, similar to that in the stretch (in)activated channels, is not currently available. However, there is qualitative structural information indicating large movement of the components as a part of conformational changes of various transporters with the in-plane dimensions reasonably close to the motor complex in outer hair cell. In the latest study (Toyoshima et al., 2000), the crystal resolution of Ca^{2+}-ATPase at 2.6 Å was achieved. The protein has 4×5 nm in-plane dimensions. The revealed structure that includes three separate domains with hinge-type connection suggests large movement of the protein domains. Wang et al. (1994) discussed "dramatic structural changes during transport" through AE1 (band 3) anion exchanger with 5.5×6 nm in-plane dimensions. Zhuang et al. (1999) mentioned "widespread conformational changes that occur during enzyme turnover" of LacY proton transporter with the in-plane dimensions 5×5.5 nm.
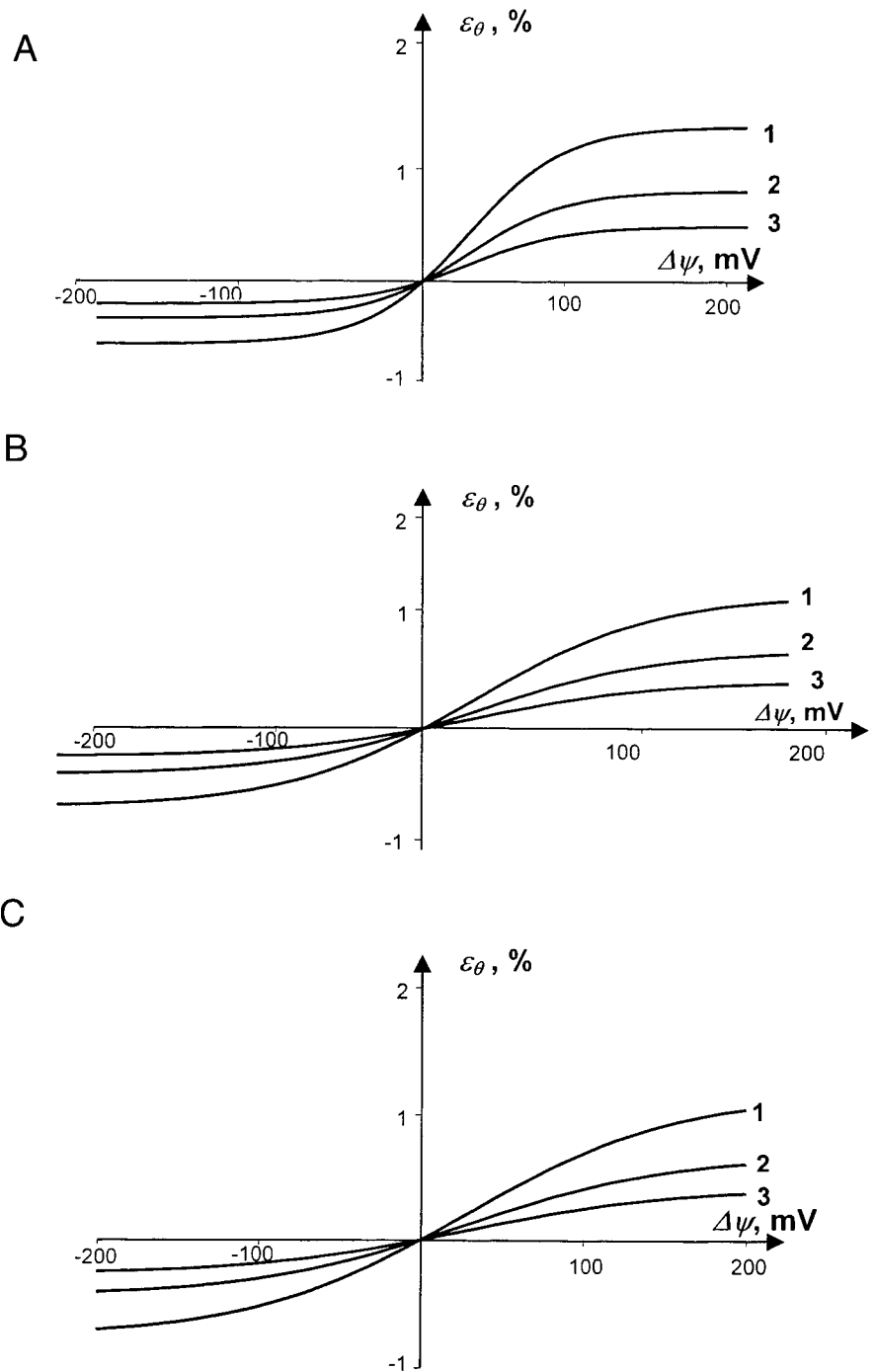
A

B

FIGURE 7 The circumferential component of the overall electromotile strain as a function of the cell wall potential for different values of the b parameter in the Boltzmann probability function of the motor being in the deformed state are considered. Also, the results for different motor densities, expressed in terms of the l edge-to-edge distance between particles, are shown. (A) $b = 30$ mV, $1 - l = 2$ nm, $2 - l = 4$ nm, and $3 - l = 6$ nm (corresponding densities of the particles are 5100, 3900, and 3090 particles per μm^2); (B) $b = 50$ mV, $1 - l = 2$ nm, $2 - l = 4$ nm, and $3 - l = 6$ nm; (C) $b = 65$ mV, $1 - l = 2$ nm, $2 - l = 4$ nm, and $3 - l = 6$ nm.

C

The longitudinal component of the active strain generated in the particle/motor complex is tensile (positive) (Eq. 26) as is the longitudinal component of the overall observable strain (Eq. 28). The circumferential component of the active strain is compressive (negative) (Eq. 26) as is the circumferential component of the overall observable strain (Eq. 28). In contrast to signs, the absolute values of our initial (active) strains are different from those of the overall observable strains (Eqs. 26 and 28). The values of the initial

(active) strain generated in the particles/motor complexes are 2–3 times greater than the resulting observable strains in the cell wall. In "free" motility that we analyze, there are no cellular-level constraints. However, our 3D modeling shows that the motor-level picture is more complicated. The motor complexes are under certain constraints because of the geometric arrangement in the plasma membrane (these constraints are mathematically expressed by the boundary conditions, Eqs. 11–16) and (to a smaller extent) the action of
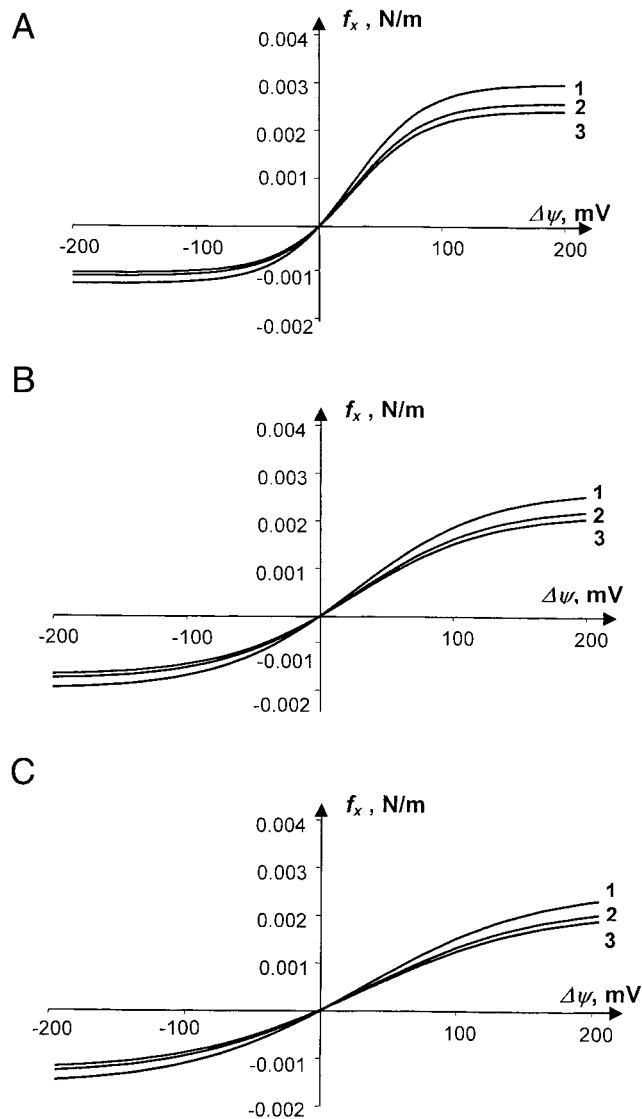
A

B

C

FIGURE 8 The longitudinal component of the active force as a function of the cell wall potential for different values of the b parameter in the Boltzmann probability function of the motor being in the deformed state are considered. Also, the results for different motor densities, expressed in terms of the l edge-to-edge distance between particles, are shown. (A) $b = 30$ mV, $1 - l = 2$ nm, $2 - l = 4$ nm, and $3 - l = 6$ nm (corresponding densities of the particles are 5100, 3900, and 3090 particles per μm^2); (B) $b = 50$ mV, $1 - l = 2$ nm, $2 - l = 4$ nm, and $3 - l = 6$ nm; (C) $b = 65$ mV, $1 - l = 2$ nm, $2 - l = 4$ nm, and $3 - l = 6$ nm.

the radial pillars. These constraints result in the interaction among the motors and generation of stress fields around them. The specific geometric arrangement in the plasma membrane is related to the wall composition as a set of identical units with one pillar and a number of particles inside. The self-balanced forces N_x and N_θ along the boundary of the unit (see Mathematical Model), necessary to provide the periodicity of the arrangement in the plasma membrane, is a manifestation of the constraints imposed on the particles/motor complexes. Such constraints lead to

larger initial strains generated in the motor complexes to provide the overall strains corresponding to those in the experiment. The discovered effect of redistribution of the motor-generated strain in the wall is an important feature of our composite 3D model. In 2D single-layer models of outer hair cell motility (e.g., Iwasa, 1994), the motor-related strains exactly coincide with the overall strains under the conditions of no external forces applied to the cell wall.

Figure 8, A–C, show the longitudinal isometric force $f_x(\Delta\Psi)$ as a function of the membrane potential for different values of the parameter b and the densities of the particles. We choose the values $f_x(200$ mV$)$ and $f_x(-200$ mV$)$ corresponding to extreme depolarization and extreme hyperpolarization for the comparison with previous estimates of the active force. These two values computed for $b = 30$ mV and $l = 2$ nm are, respectively, $\sim$38 and 45% smaller than the estimates previously obtained on the basis of a continuum approach (Spector, 2001; Spector et al., 1999). Note that experimental ranges for active force give several times and even an order of magnitude variation (see discussion in Spector et al., 1999).

The longitudinal stiffness of the cell wall is characterized by the coefficient C_{11}. This modulus was previously estimated in Spector et al. (1998b). The current computational model results in modulus $C_{11} = 0.11$ N/m, which is about 45% smaller than that in Spector et al. (1998b).

The computed moduli of the components of the plasma membrane correspond to the small compressibility of the material around particles with area expansion modulus three orders of magnitude greater than shear modulus (Eq. 25). Also, the material of the particles is much stiffer than that around particles with the ratio of corresponding Young's moduli equal to 20 (Eq. 27). This satisfies criterion 5 formulated above.

The level of incompressibility of the material around particles expressed in terms of Poisson's ratio ν^3 is one of the parameters in our model. The properties of the material surrounding the particles in the plasma membrane are, probably, different from those for a pure lipid bilayer. The reason for this difference is the presence of the particles and other intramembranous proteins. It is known (Kim et al., 1998) that the properties of the lipid bilayer are altered by the presence of embedded proteins because of the interaction among them. Such an alteration can be significant in the case of the outer hair cell plasma membrane because of the high density of the embedded particles.

The characteristics of the cell wall active properties presented in Figs. 6, A–C, 7, A–C, and 8, A–C are given for three densities of the particles/motor complexes. For the diameter of the particle equal to 12 nm, the considered range $l = 2$–6 nm corresponds to a range in the density of the particles about 3000–5000 per μm^2. Forge (1991) estimated the density of the particles as 6000 per μm^2. Kalinec et al. (1992) and Saito (1983) reported densities 2000–3000 per μm^2. Santos-Sacchi et al. (1998) estimated the density of

the particles in the plasma membrane for cells of different lengths. They found the density about 4000 per μm^2 in longer (low frequency) cells and 4800 per μm^2 in shorter (high frequency) cells. Our results show a significantly lower electromotile response for lower density of the particles (curves 3 versus curves 1 in Figs. 6, A–C and 7, A–C). However, the corresponding differences in the active force are much smaller (curves 1 versus curves 3 in Fig. 8, A–C). Smaller differences in the values of the active force can be explained by the interplay between the components of the active strain and the passive stiffness, major determinants of the active force. We have shown that the density of the particles/motor complexes affects the active strain produced by the cell wall. The density of the particles whose stiffness is different from that of the lipid bilayer also affects the stiffness of the plasma membrane, which causes changes in the longitudinal and circumferential stiffness (stiffness moduli) of the whole wall. Thus, a combination of these density-related changes results in a smaller variability of the active force compared to that of the active strain.

Theoretical estimates obtained on the basis of the proposed model can stimulate future experimental studies of the molecular motors and the mechanism of transduction of the active strain from the plasma membrane to the cytoskeleton. The dimensional changes of an individual motor complex and the motor complex stiffness predicted, respectively, by Eqs. 26 and 27 can be tested when more detailed information on the Prestin molecule becomes available. Also, a weak effect of the connection between the plasma membrane and the cytoskeleton demonstrated by the data in Table 1 can be further tested in the experiment with partially destroyed radial pillars.

In summary, we propose a 3D model of the outer hair cell wall that explicitly takes into account available nanostructural information on the composite cell wall. Our model includes lipid–protein interactions within the plasma membrane as well as the interaction between the plasma membrane and the passive components (cytoskeleton and subsurface cisternae) of the cell wall. We estimate the parameters of our model from the requirement that the results of our simulation match experimental observations and previously obtained theoretical results. We apply the proposed model to the analysis of the mechanism of electromotility that includes the interaction among the wall components both through the wall thickness and along the plasma membrane. Our analysis revealed a number of biophysical features of the active strain and force production previously unavailable to either experimental observation or single-layer mathematical models. The developed 3D computational model can be an effective complement and aid to experimental studies of electromotility. The model is built as a set of assembled modules, such as cytoskeleton, pillars, particles/motor complexes, etc. It will allow molecular-level developments of the model when new information on the cell components becomes available. As one example, the

future information on the relative motion, rotation, and translation of the motor complex elements can be incorporated by changing the model representation of the particles. As another example, a modification of the representation of the lipid bilayer can be used in the interpretation of the recently discovered voltage- and tension-dependent lipid mobility in the outer hair cell plasma membrane (Oghalai et al., 2000). The model can also be used for a more accurate estimation of the outer hair cell active force production in the organ of Corti and for the rational bridge between the local active and passive properties measured in isolated cells and the outer hair cell behavior under physiological conditions.

REFERENCES

Ashmore, J. F. 1990. Forward and reverse transduction in the mammalian cochlea. *Neurosci. Res. Suppl.* 12:S39–S50.

Adachi, M., and K. H. Iwasa. 1999. Electrically driven motor in the outer hair cell: effect of a mechanical constraint. *Proc. Natl. Acad. Sci. U.S.A.* 96:7244–7249.

Belyantseva, I. A., H. J. Adler, R. Curi, G. I. Frolenkov, and B. Kachar. 2000. Expression and localization of Prestin and sugar transporter Glut-5 during development of electromotility in cochlear outer hair cells. *J. Neurocsi.* 20:RC116(1–5).

Brownell, W. E., C. R. Bader, D. Bertrand, and Y. de Ribaupierre. 1985. Evoked mechanical responses of isolated cochlear outer hair cells. *Science.* 227:194–196.

Brownell, W. E., and A. S. Popel. 1998. Electrical and mechanical anatomy of the outer hair cell. *In* Psychological and Physiological Advances in Hearing. A. R. Palmer, A. Rees, A. Q. Summerfield, and R. Meddis, editors. Whurr Publishers Ltd., London, 89–96.

Brownell, W. E., A. A. Spector, R. M. Raphael, and A. S. Popel. 2001. Micro- and nanomechanics of the cochlear outer hair cell. *Ann. Rev. Biomed. Eng.*, in press.

Dallos, P., R. Hallworth, and B. N. Evans. 1993. Theory of electrically driven shape changes of cochlear outer hair cells. *J. Neurophys.* 70: 299–323.

Cook, R. D., D. D. Malkus, and M. E. Plesha. 1989. Concept and applications of finite element analysis. John Wiley & Sons, New York.

Evans, B. N., and P. Dallos. 1993. Stereocilia displacement induced somatic motility of cochlear outer hair cells. *Proc. Natl. Acad. Sci. U.S.A.* 90:8347–8351.

Frank, G., W. Hemmert, and A. W. Gummer. 1999. Limiting dynamics of high-frequency electromechanical transduction of outer hair cells. *Proc. Natl. Acad. Sci. U.S.A.* 96:4420–4425.

Forge, A. 1991. Structural features of the lateral walls in mammalian cochlear outer hair cells. *Cell Tissue Res.* 265:473–484.

Gale, J. E., and J. F. Ashmore. 1997. The outer hair cell motor in membrane patches. *Pflugers Arch.* 434:267–271.

Geleoc, G. S. G., S. O. Casalotti, A. Forge, and J. F. Ashmore. 1999. A sugar transporter as a candidate for the outer hair cell motor. *Nature Neurosci.* 2:713–719.

Hallworth, R., B. N. Evans, and P. Dallos. 1993. The location and mechanism of electromotility in guinea pig outer hair cell. *J. Neurophys.* 70:549–558.

Holley, M. C. 1996. Outer hair cell motility. *In* The Cochlea. P. Dallos, A. N. Popper, and R. R. Fay, editors. Springer-Verlag, New York. 386–434.

Holley, M. C., F. Kalinec, and B. Kachar. 1992. Structure of the cortical cytoskeleton in mammalian outer hair cells. *J. Cell. Sci.* 102:569–580.

Huang, G. and Santos-Sacchi, J. 1994. Motility voltage sensor of the outer hair cell resides within the lateral plasma membrane. *Proc. Natl. Acad. Sci. U.S.A.* 91:12268–12272.

Iwasa, K. H. 1994. A membrane motor model for the fast motility of the outer hair cell. *J. Acoust. Soc. Am.* 96:2216–2224.

Iwasa, K. H. 1996. Membrane motor in the outer hair cell of the mammalian ear. *Comments Theor. Biol.* 4:94–114.

Jen, D. H., and C. R. Steele. 1987. Electro-kinetic model of outer hair cell motility. *J. Acoust. Soc. Am.* 82:1667–1678.

Kalinec, F., M. C. Holley, K. H. Iwasa, D. J. Lim, and B. Kachar. 1992. A membrane-based force generation mechanism in auditory sensory cells. *Proc. Natl. Acad. Sci. U.S.A.* 89:8671–8675.

Kalinec, F., and B. Kachar. 1995. Structure of the electromechanical transduction mechanism in mammalian outer hair cells. *In* Active Hearing. A. Flock, D. Ottoson, and M. Ulfendahl, editors. Elsevier, Amsterdam, 179–191.

Kim, K. S., J. Neu, and G. Oster. 1998. Curvature-mediated interactions between membrane proteins. *Biophys. J.* 75:2274–2291.

Love, A. E. H. 1952. A Treatise on the Mathematical Theory of Elasticity, 4th Ed., Dover, New York.

Ludwig, J., D. Oliver, G. Frank, N. Klöcker, A. W. Gummer, and B. Fakler. 2001. Reciprocal electromechanical properties of rat prestin: the motor molecule from rat outer hair cells. *Proc. Natl. Acad. Sci. U.S.A.* 98:4178–4183.

Mammano, F., and J. F. Ashmore. 1993. Reverse transduction measured in the isolated cochlea by laser Michelson interferometry. *Nature.* 365:838–841.

Morris, C. E. 1990. Mechanosensitive ion channels. *J. Membr. Biol.* 113:93–107.

Oghalai, J. S. H.-B. Zhao, J. W. Kurz, and W. E. Brownell. 2000. Voltage- and tension-dependent lipid mobility in the outer hair cell plasma membrane. *Science.* 287:658–661.

Raphael, R. M., A. S. Popel, and W. E. Brownell. 2000. A membrane bending model of outer hair cell electromotility. *Biophys. J.* 78:2844–2862.

Ratnanather, J. T., A. A. Spector, A. S. Popel, and W. E. Brownell. 1997. Is the outer hair cell viscoelastic? *In* Diversity in Auditory Mechanics. E. R. Lewis, G. R. Long, R. F. Lyon, P. M. Naryns, C. R. Steele, and E. Hetcht-Poinar, editors. World Scientific, Singapore. 601–607.

Ruggero, M. A. and N. C. Rich. 1991. Furosemide alters organ of Corti mechanics: evidence for feedback of outer hair cells upon the basilar membrane. *J. Neurosci.* 11:1057–1067.

Saito, K. 1983. Fine structure of the sensory epithelium of guinea pig organ of Corti: subsurface cisternal and lamellar bodies of the outer hair cells. *Cell Tissue Res.* 229:467–481.

Santos-Sacchi, J., and J. P. Digler. 1988. Whole cell current and mechanical responses of isolated outer hair cell. *Hearing Res.* 35:143–150.

Santos-Sacchi, J., S. Kakehata, T. Kikuchi, Y. Katory, and T. Takasaka. 1998. Density of motility-related charge in the outer hair cell of the guinea pig is inversely related to best frequency. *Neurosci. Lett.* 256:155–158.

Spector, A. A. 2001. A nonlinear electroelastic model of the auditory outer hair cell. *Int. J. Solids Struct.* 38:2115–2129.

Spector, A. A., M. Ameen, P. G. Charalambides, and A. S. Popel. 2000. Computational modeling of the outer hair cell cytoskeleton. *In* Recent Developments in Auditory Mechanics. H. Wada, T. Takasaka, K. Ikeda, K. Ohuama, and T. Koike, editors, World Scientific Publishing, Singapore, 307–313.

Spector, A. A., W. E. Brownell, and A. S. Popel. 1998a. Elastic properties of the composite outer hair cell wall. *Ann. Biomed. Eng.* 26:157–165.

Spector, A. A., W. E. Brownell, and A. S. Popel. 1998b. Estimation of elastic moduli and bending stiffness of anisotropic outer hair cell wall. *J. Acoust. Soc. Am.* 103:1007–1011.

Spector, A. A., W. E. Brownell, and A. S. Popel. 1999. Nonlinear active force generation by cochlear outer hair cell. *J. Acoust. Soc. Am.* 105:2414–2420.

Sukharev, S., M. Betanzos, C.-S. Chiang, and H. R. Guy. 2001. The gating mechanism of the large mechanosensitive channel Mscl. *Nature.* 409:720–724.

Tolomeo, J. A., C. R. Steele, and M. C. Holley. 1996. Mechanical properties of the lateral cortex of mammalian auditory outer hair cells. *Biophys. J.* 71:421–429.

Tolomeo, J. A. and R. C. Steele. 1998. A dynamic model of outer hair cell motility including intracellular and extracellular fluid viscosity. *J. Acoust. Soc. Am.* 103:524–534.

Toyoshima, C., M. Nakasako, H. Nomura, and H. Ogawa. 2000. Crystal structure of the calcium pump of sarcoplasmic reticulum at 2.6 Å resolution. *Nature.* 405:647–655.

Xue, S., D. C. Mountain, and A. E. Hubbard. 1993. Direct measurements of electrically evoked basilar membrane motion. *In* Biophysics of Hair Cell Sensory Systems, H. Duinfuis, J. W. Horst, P. van Dijk, and S. M. van Netten, World Scientific Publishing, Singapore, 361–368.

Wang, D. N., V. E. Sarabia, A. F. Reithmeier, and W. Kuhlbrandt. 1994. Three-dimensional map of the dimeric membrane domain of the human erythrocyte anion exchanger, Band 3. *EMBO J.* 13:3230–3235.

Zheng, J., W. Shen, D. He, K. B. Long, L. D. Madison, and P. Dallos. 2000. Prestin is the motor protein of cochlear outer hair cells. *Nature.* 405:149–155.

Zhuang, J., G. G. Prive, G. E. Werner, P. Ringler, H. R. Kaback, and A. Engel. 1999. Two-dimensional crystallization of *Escherichia coli* Lactose Permease. *J. Struct. Biol.* 125:63–75.